Response, Localization, and Rupture of Anisotropic Tubes Under Combined Pressure and Tension

Martin Scales[1]
Research Center for Mechanics of Solids, Structures & Materials, The University of Texas at Austin, ASE, 2617 Wichita Street, Austin, TX 78712
e-mail: mscales@exponent.com

Kelin Chen[2]
Research Center for Mechanics of Solids, Structures & Materials, The University of Texas at Austin, ASE, 2617 Wichita Street, Austin, TX 78712
e-mail: kelinchen@utexas.edu

Stelios Kyriakides[3]
Research Center for Mechanics of Solids, Structures & Materials, The University of Texas at Austin, ASE, 2617 Wichita Street, Austin, TX 78712
e-mail: skk@mail.utexas.edu

The inelastic response and failure of Al-6061-T6 tubes under combined internal pressure and tension is investigated as part of a broader study of ductile failure of Al-alloys. A custom experimental setup is used to load thin-walled tubes to failure under radial paths in the axial-hoop stress space. All loading paths achieve nominal stress maxima beyond which deformation localizes into a narrow band. 3D digital image correlation (DIC) was used to monitor the deformations in the test section and successfully captured the rapid growth of strain within the localization bands where they burst. The biaxial stress states generated are first used to calibrate the nonquadratic anisotropic Yld04-3D yield function (Barlat et al., 2005, "Linear Transformation-based Anisotropic Yield Functions," Int. J. Plasticity, 21(5), pp. 1009–1039). The constitutive model is then incorporated through a UMAT into a finite element analysis and used to simulate numerically the experiments. The same calculations were performed using von Mises (VM) and an isotropic nonquadratic yield function. The material hardening responses adopted were extracted for each constitutive model from the necked zone of a tensile test using an inverse method. The use of solid elements captures the evolution of local deformation deep into the localizing part of the response, producing strain levels that are required in the application of failure criteria. The results demonstrate that the adoption of a nonquadratic yield function, together with a correct material hardening response are essential for large deformation predictions in localizing zones in Al-alloys. Including the anisotropy in such a constitutive model produces results that are closest to the experiments. [DOI: 10.1115/1.4048648]

Keywords: burst failure of tubes, combined tension and pressure, anisotropy, material hardening, constitutive modeling of materials, flow and fracture, plasticity

1 Introduction

The response and rupture of Al-6061-T6 tubes under combined internal pressure and tension is investigated as part of a broader study on ductile failure of aluminum alloys (e.g., Refs. [1–3]). Thin-walled tubes extracted from the same tubular stock as the rest of the tubes used in the study were tested to failure by burst under radial paths in the nominal hoop and axial stress space. The experiments are similar to a certain degree to those in Ref. [4] (see also Refs. [5,6]). However, in the present experiments, the use of high resolution 3D digital image correlation (DIC) to monitor the deformation of the test section allows accurate measurement of both the induced average biaxial strain and the localized deformation that leads to rupture.

The biaxial stress states generated are first used to calibrate the nonquadratic anisotropic Yld04-3D yield function of Barlat et al. [7]. The calibrated constitutive model is then incorporated through a UMAT into a custom finite element analysis, which is used to simulate numerically the experiments. Simulations using the classical von Mises (VM) and a nonquadratic isotropic model are also performed. Unlike prior numerical efforts involving combined tension and internal pressure, solid elements are used to discretize the structure. Solid elements enable monitoring of the evolution of local deformation deeply into the post-limit load localizing part of the response producing strain levels that are required in the application of failure criteria. Another important component of the analysis is the use of hardening responses extracted for each of the three constitutive models from the necked zone of a tensile test on an axial strip using the inverse method of Tardif and Kyriakides [8].

The results are used to demonstrate the effect of anisotropy on the responses in this biaxial setting, but even more importantly the effect of the constitutive model on the evolution of deformation in the narrow neck that forms following the limit load that results in failure.

2 Experimental Setup, Procedures, and Results

The pressure-tension experiments involved 12 in (305 mm) long tubular specimens extracted from the same 2-in (51 mm) diameter, 0.187 in (4.75 mm) wall thickness seamless tubular stock used in the tension-torsion failure study in Ref. [2]. A 4.0 in (102 mm) long test section with a nominal outer diameter of 1.73 in (43.9 mm) and a wall thickness of 0.050 in (1.27 mm) was machined in the center of the test tube. The thicker end sections were sealed with solid plugs and the assembly was mounted in a servo-hydraulic testing machine using custom housings and pressurized clamps as shown in Fig. 1. Axial load is applied by the 50 kip (222 kN) test machine, and pressure via an independent 10,000 psi (690 bars) closed-loop pressurizing system. The two systems are connected through feedback, which enables the tracing of radial paths in the nominal axial stress-hoop stress space as follows:

$$\Sigma_x = \eta\Sigma_\theta, \quad \eta = \text{const.} \tag{1}$$

The nominal stresses are related to the applied pressure P and axial force F through

[1]Present address: Exponent, Inc., 3350 Peachtree Road NE, Suite 1620, Atlanta, GA 30326.
[2]Present address: Department of Integrated Systems Engineering, The Ohio State University, 210 Baker Systems, Columbus, OH 43210.
[3]Corresponding author.
Manuscript received September 3, 2020; final manuscript received September 30, 2020; published online October 27, 2020. Assoc. Editor: Yonggang Huang.

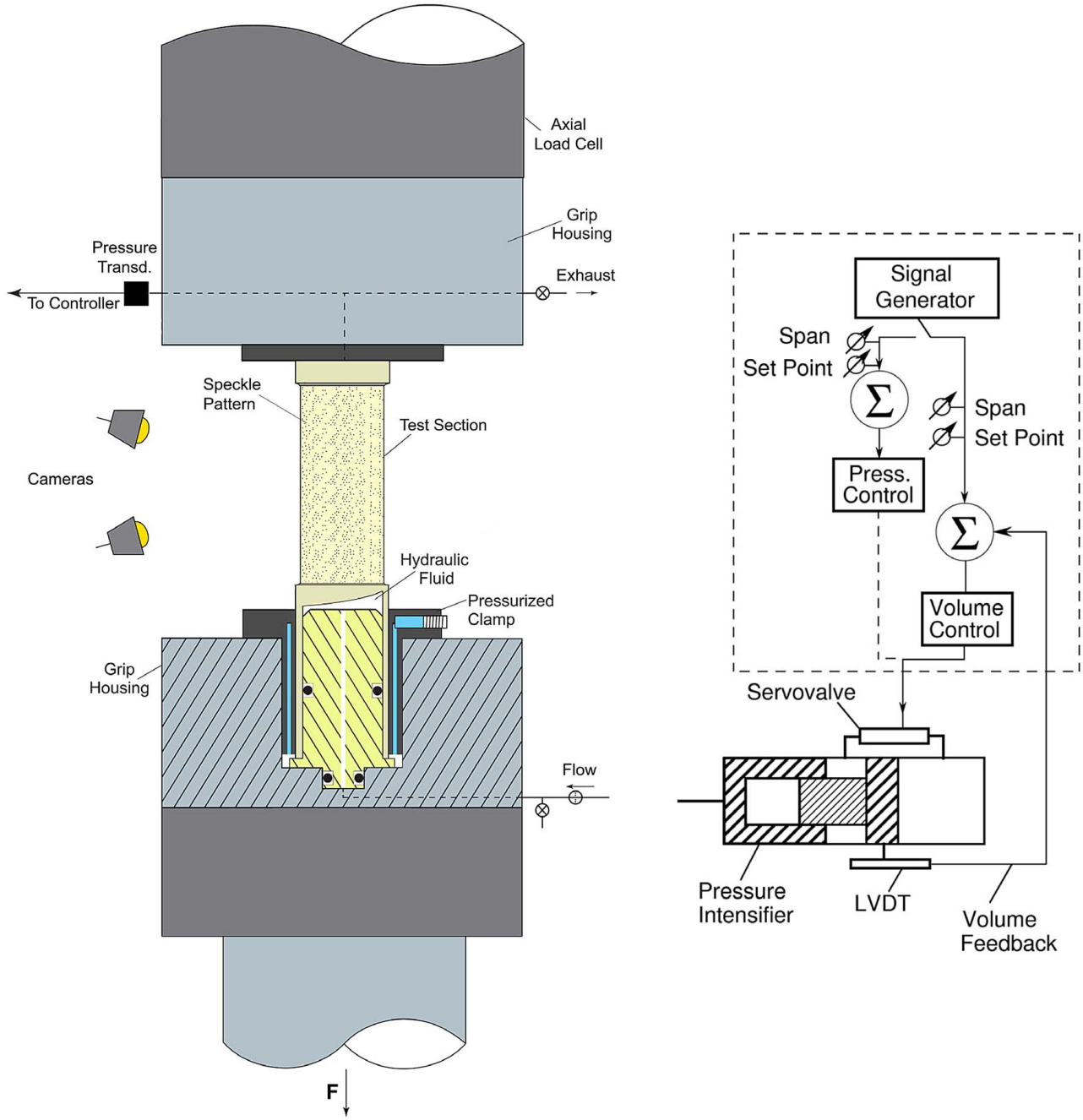

Fig. 1 Schematic of the pressure-tension experimental setup on the left and the closed-loop controlled pressurizing system on the right

$$\Sigma_\theta = \frac{PR_o}{t_o} \quad \text{and} \quad \Sigma_x = \frac{F}{2\pi R_o t_o} + \frac{PR_o}{2t_o} \tag{2}$$

where R_o and t_o are the initial mid-surface radius and thickness. The desired radial path is achieved by operating the pressurizing system in volume control, and using the pressure as a command signal for the axial force (loading scheme similar to that in Ref. [9]). The volume was prescribed at a slow rate that resulted in an equivalent strain rate of the order of 10^{-3} s^{-1} during the homogeneous deformation stage of the experiment (note that Al-6061-T6 exhibits very mild strain rate sensitivity which is negligible at such slow rates).

The test section deformation was continuously monitored using 3D DIC. Our system employs two 5 MP digital cameras equipped with 50 mm lenses.

The cameras were oriented vertically so that the full length of the test section, and nearly 180 deg of the circumference, could be monitored. The strains were *averaged* over the central 1 in (25.4 mm) length and 90 deg sector. Correlation and the instantaneous logarithmic strains (ε_x, ε_θ) were computed using GOM ARAMIS v 6 using a facet size of 15 pixels and a spacing of 5 pixels corresponding to approximately $0.6t_o$ and $0.2t_o$. These measurements are used to obtain a first estimate of the current wall thickness $t = t_o \exp(-\varepsilon_x - \varepsilon_\theta)$. This value of t is used to obtain a first estimate of the true stresses (σ_x, σ_θ), which are then used to establish the plastic components of the strains and the through-thickness component $\varepsilon_r^p = -(\varepsilon_x^p + \varepsilon_\theta^p)$. This produces a new estimate of ε_r and the process is repeated leading to quick (usually) convergence in the stresses.

2.1 Experimental Results. Seven pressure-tension radial path experiments were performed with stress ratios $\eta = \{0, 0.25, 0.5,$

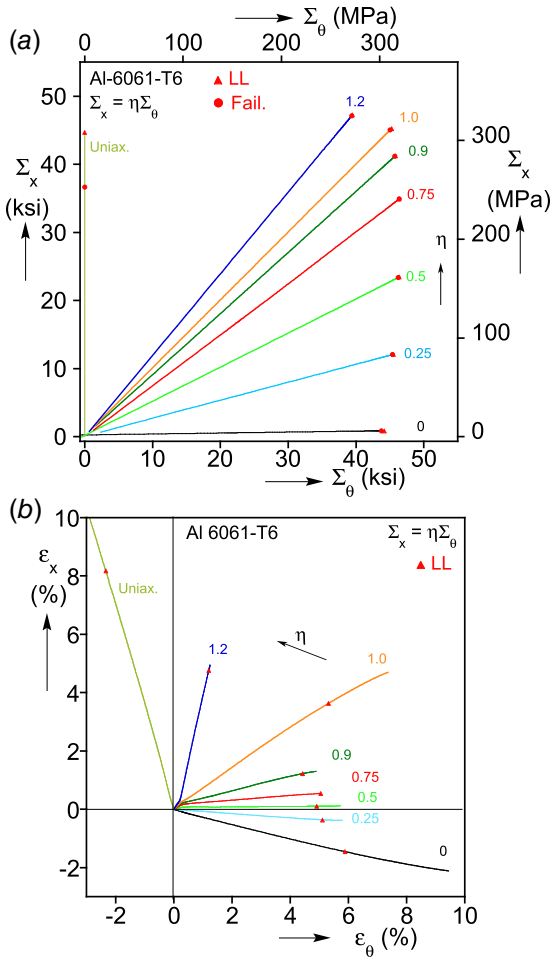

Fig. 2 (*a*) Nominal stress histories of the seven P-T tests, and one uniaxial tension test and (*b*) recorded average strain histories.

0.75, 0.9, 1.0, 1.2} as shown in Fig. 2(*a*). Table 1 lists the main geometric characteristics of each test specimen. Figure 3(*a*) shows the recorded nominal hoop stress-average logarithmic hoop strain ($\Sigma_\theta - \varepsilon_\theta$) responses, and Fig. 3(*b*) the corresponding axial responses ($\Sigma_x - \varepsilon_x$). Each experiment achieves a load maximum (indicated by ▲) beyond which deformation localizes, first as a mild bulge at mid-span, and subsequently in the form of a narrow axial neck with a width of the order of the wall thickness. The neck quickly deepens and causes rupture by burst. Such burst failures were sudden and catastrophic, but the "stiff" test setup of our system limited the axial extent of the rupture. For $\eta = 1.2$, deformation localized instead as a narrow circumferential band that ruptured separating the specimen in two.

The stress levels of the hoop direction responses in Fig. 3(*a*) are banded together, whereas the axial stress levels in Fig. 3(*b*) fall in accordance with the value of η. Figure 2(*b*) plots the induced logarithmic strain histories, which are essentially linear up to the limit load and mildly nonlinear beyond. The average strain levels are smaller for η of 0.5 and 0.75 and larger for $\eta = 0$, 1.0, and 1.2. The nominal stresses and strains at the limit load (subscript L) are listed in Table 1. Included are also the nominal stresses from the last data recorded before failure (subscript f). The failure strains reported are the largest values extracted from within the localization band from the last DIC image recorded. Consequently, they are significantly larger than the average values at the end of the strain trajectories in Fig. 2(*b*).

The evolution of localization is now illustrated using results from the $\eta = 0.25$ experiment. Figure 4(*a*) shows isolated the ($\Sigma_\theta - \varepsilon_\theta$) response with five stations marked with numbered bullets. Figure 4(*b*) plots the equivalent strain along a circumferential profile that crosses the localization zone at these five stations. Station ② at a hoop strain of 5.12% corresponds to the limit load. For station ① with the much lower strain of 2.55%, the profile is essentially flat indicating that the deformation is uniform around the circumference. At the pressure maximum, a clear increase in strain that covers a span of about $3t_o$ is observed. The strain achieved a maximum value of 0.14 whereas away from this zone it is at about 0.053—corresponds to the average value in Fig. 4(*a*). In stations ③, ④, and ⑤ at average strains of 0.0535, 0.0559, and 0.0579, the local strain progressively increases with the growth now being concentrated in a span of about $2t_o$. A thickness depression formed at the apex of the protrusion, and in the last image recorded by DIC before burst the strain reaches a maximum value of 0.26. Concurrently, the strain away from this zone remained essentially unchanged for all four stations. The equivalent strain recorded at the point undergoing the maximum deformation is plotted against the average hoop strain in Fig. 5. The trajectory demonstrates the nearly exponential growth of local strain around and beyond the limit load—marked with ▲. Note that $e_e - \varepsilon_\theta$ trajectories from the rest of the experiments in the set included in the figure exhibit the same rapid growth in the local strain as rupture is approached. For this reason, in the experiments, the last few images were taken at 1 s intervals. Thus, although the results capture the trend of events, because of the accelerated unstable growth of localized deformation as failure is approached, the actual maximum strain at failure was not captured and is expected to be much larger. Figure 6(*a*) shows DIC contours from the last image recorded in the $\eta = 0.25$ experiment and Fig. 6(*b*) shows the burst specimen. The rupture extends over a length of $0.6D$ and the fracture surface is inclined at an angle of about 45 deg.

3 Analysis

The experiments are simulated numerically using solid elements in order to follow the evolution of the axial localization zone that precedes rupture. As in our preceding works on the response and

Table 1 Biaxial experiments: geometry of test specimens, and stresses and strains at the limit loads and at failure

Exp. no.	η	R mm (in)	t mm (in)	Ξ_o (%)	Σ_{xL}(MPa) (ksi)	$\Sigma_{\theta L}$(MPa) (ksi)	ε_{xL} (%)	$\varepsilon_{\theta L}$ (%)	Σ_{xf}(MPa) (ksi)	$\Sigma_{\theta f}$(MPa) (ksi)	ε_{xf} (%)	$\varepsilon_{\theta f}$ (%)
11	0	21.3 (0.839)	1.26 (0.0498)	2.29	6 (0.9)	305 (44.2)	−1.45	5.89	6 (0.9)	302 (43.8)	−1.33	24.59
12	0.25	21.3 (0.839)	1.26 (0.0497)	2.50	83 (12.1)	314 (45.5)	−0.36	5.12	83 (12.0)	313 (45.4)	−0.37	23.06
4	0.5	21.3 (0.839)	1.26 (0.0498)	2.48	162 (23.4)	320 (46.4)	0.10	4.92	161 (23.4)	319 (46.2)	0.22	21.14
2	0.75	21.3 (0.839)	1.26 (0.0498)	2.60	241 (34.9)	320 (46.4)	0.54	5.06	241 (34.9)	320 (46.4)	1.47	17.40
3	0.9	21.3 (0.839)	1.27 (0.0501)	2.90	284 (41.2)	316 (45.8)	1.22	4.44	284 (41.2)	315 (45.7)	1.78	20.38
8	1	21.3 (0.839)	1.26 (0.0496)	4.52	312 (45.3)	312 (45.3)	3.63	5.32	311 (45.0)	311 (45.0)	4.88	21.30
10	1.2	21.2 (0.834)	1.01 (0.0399)	4.36	326 (47.3)	272 (39.5)	4.77	1.21	325 (47.1)	272 (39.4)	24.81	2.19

$\Sigma_x = \eta\Sigma_\theta$.

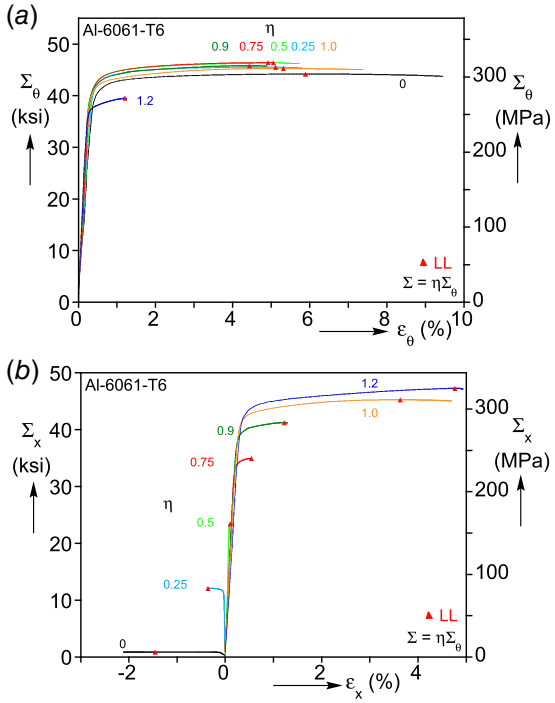

Fig. 3 Nominal stress-average strain responses of the seven P-T experiments: (*a*) hoop and (*b*) axial results

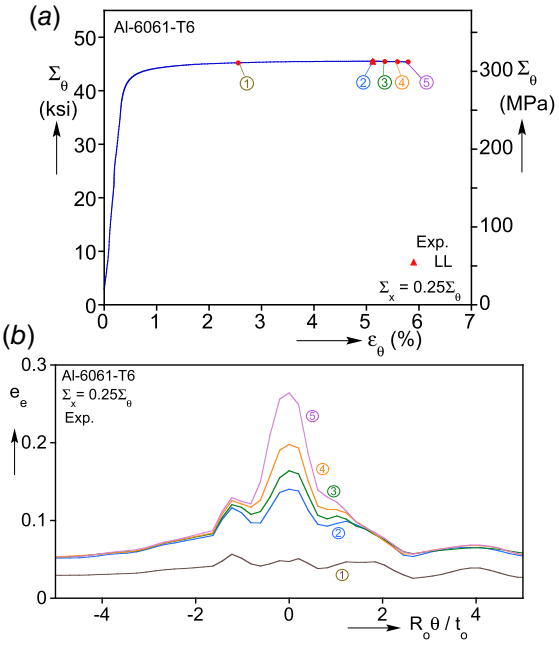

Fig. 4 (*a*) Nominal hoop stress-average strain response for the $\eta = 0.25$ experiment; station ② is the limit load. (*b*) Equivalent strain profiles across the localization zone at the five stations marked in (*a*).

ductile failure under multiaxial loads, three constitutive models are adopted: (a) the first is based on the quadratic VM yield function; (b) one based on the nonquadratic yield function of Hosford [10], which in terms of the principal deviatoric stress components can be expressed as

$$\Phi = [(|s_1 - s_2|^k + |s_2 - s_3|^k + |s_3 - s_1|^k)/2]^{1/k} \tag{3}$$

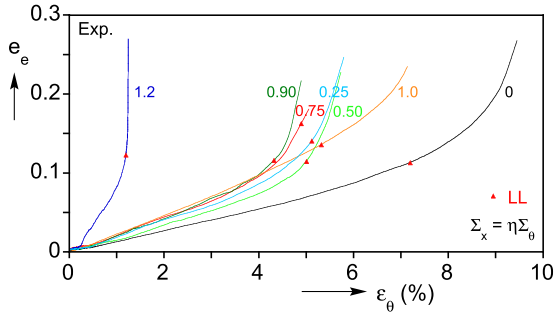

Fig. 5 Maximum equivalent strain recorded in the localization zone versus average hoop strain for the seven P-T experiments

and (c) the nonquadratic anisotropic 3D yield function of Balat et al. [7] Yld04-3D, expressed as

$$\Phi = [(|S'_1 - S''_1|^k + |S'_1 - S''_2|^k + |S'_1 - S''_3|^k + |S'_2 - S''_1|^k + |S'_2 - S''_2|^k + |S'_2 - S''_3|^k + |S'_3 - S''_1|^k + |S'_3 - S''_2|^k + |S'_3 - S''_3|^k])/4]^{1/k} \tag{4}$$

where S' and S'' are linear transformations of the Cauchy stress tensor through which orthotropic anisotropy is introduced (results in 18 anisotropy parameters (see Refs. [3,7]; see also Ref. [11] who used an extended version of Yld02-2D with fewer anisotropy constants in solid element calculations). The stresses and strains from the uniaxial and seven biaxial experiments were used to calibrate the model as outlined in Appendix A, and the determined constants are listed in Table 2. Because the stress state in the experiments was limited to the (x, θ) plane, six of the constants could not be determined and were assigned values of 1.0.

The material hardening response was measured using a tensile test on an axial dogbone specimen from the same tube stock as the biaxial test specimens. Since tensile tests lead to necking at relatively small strains, the hardening at larger strains is extracted using

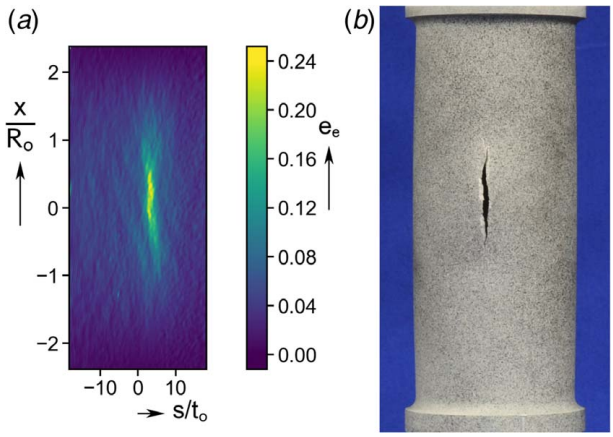

Fig. 6 (*a*) Equivalent strain contour in the last stage prior to failure for the $\eta = 0.25$ experiment and (*b*) photograph showing the same specimen after rupture

Table 2 Anisotropy parameters for Yld04-3D constitutive model

c'_{12}	c'_{13}	c'_{21}	c'_{23}	c'_{31}	c'_{32}	$c'_{44,55,66}$
−0.2846	0.4221	0.7066	0.6257	−2.0404	−1.3176	1.0
c''_{12}	c''_{13}	c''_{21}	c''_{23}	c''_{31}	c''_{32}	$c''_{44,55,66}$
−0.0378	0.2290	0.1698	0.0841	−0.9810	−2.4454	1.0

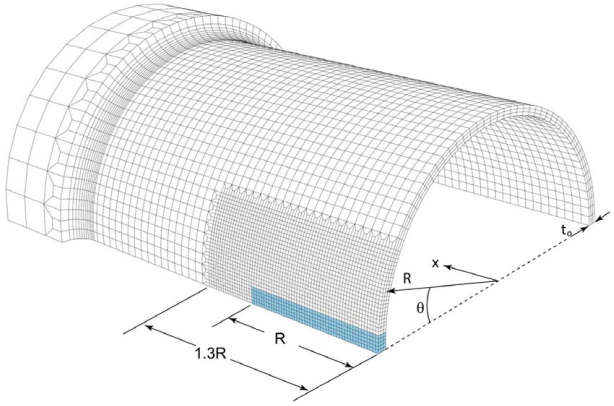

Fig. 7 Finite element model and mesh adopted for simulation of the pressure dominant P-T experiments

an inverse method that combines the constitutive model with the finite element modeling to match the measured force–displacement response as described in Appendix B (see also, Ref. [8]). The hardening response extracted for each of the three constitutive models appears in Fig. 20(*b*).

The finite element model used to simulate numerically the six pressure-tension experiments that developed an axially oriented rupture is shown in Fig. 7. Assuming symmetry about the mid-length, and about a plane that contains the axis of the tube and the zone of rupture enables consideration of only one-fourth of the structure. The model includes one half of the 4-in long test section and part of the thicker section that protruded outside the grips in the experiments (see Fig. 1). A small axial thickness depression imperfection is introduced at the plane of symmetry shown

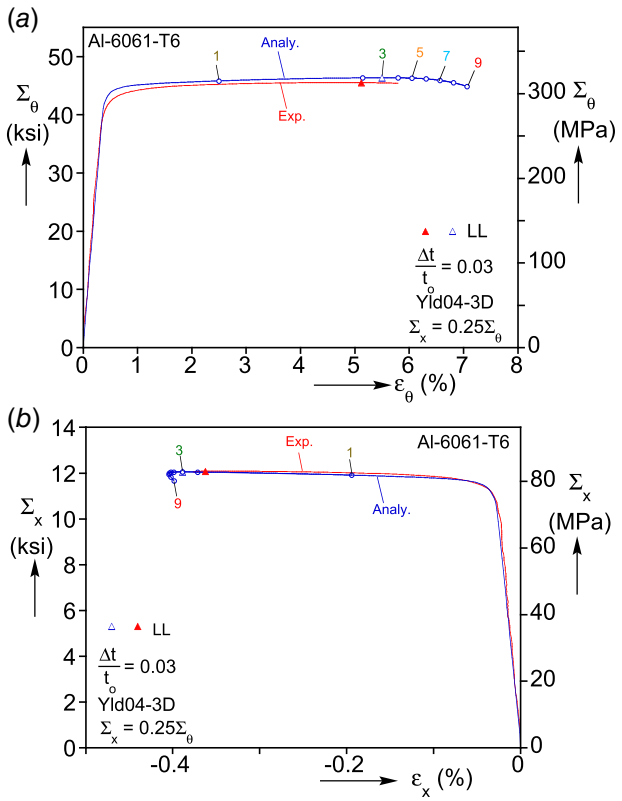

Fig. 8 Nominal stress-average strain responses for the $\eta = 0.25$ experiment and Yld04 analysis: (*a*) hoop and (*b*) axial direction results

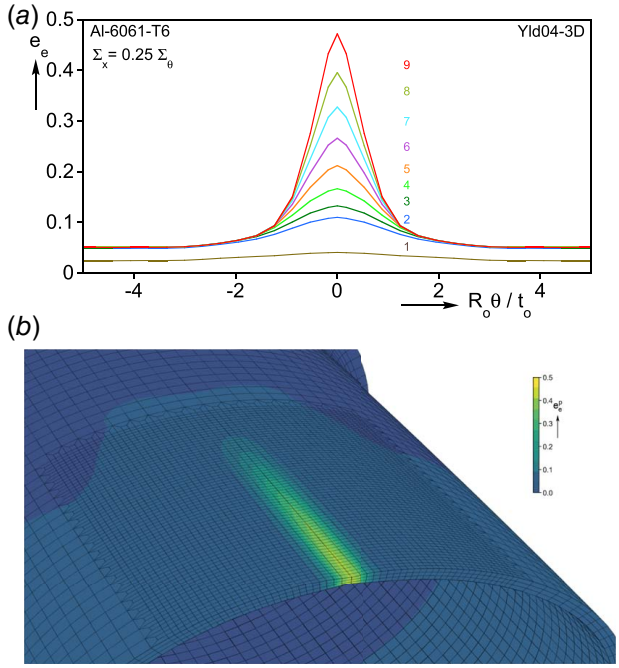

Fig. 9 (*a*) Calculated equivalent strain profiles across the localization zone predicted by the Yld04 model at the nine stations marked in Fig. 8 for the $\eta = 0.25$ experiment; station ③ corresponds to the limit load in the analysis. (*b*) Close-up view of the localization at station ⑨.

colored in the figure. It has a width of $2t_o$, length of R and, a circumferential cosine distribution with amplitude Δt. The domain is meshed with ABAQUS' solid linear elements (C3D8R). The whole domain has three elements through the thickness—this may require further refinement when performing failure calculations that go deeper in the localizing zone than was achieved in the experiments. The straight test section has 51 elements around the circumference, and 40 along the length. A zone $1.3R$ long and angular span of 30 deg around the imperfection has a finer mesh with 66 elements along the length and 27 elements in the circumferential direction. The mesh of the radiused fillet is also refined while that of the thicker section at the end is made coarser. Nodes on the $x = 0$ plane of symmetry are constrained in the axial direction but are free in the radial direction. Nodes across the thickness surface of the thicker end are kinematically coupled to a reference node to facilitate the axial motion.

The loading mimics that of the experiments. The model is pressurized under volume control using incompressible fluid elements

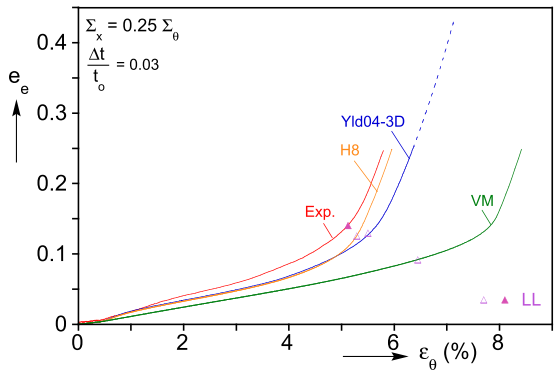

Fig. 10 Measured equivalent strain in the localizing zone versus the average hoop strain for $\eta = 0.25$ and corresponding predictions using the VM, H8, and Yld04-3D constitutive models

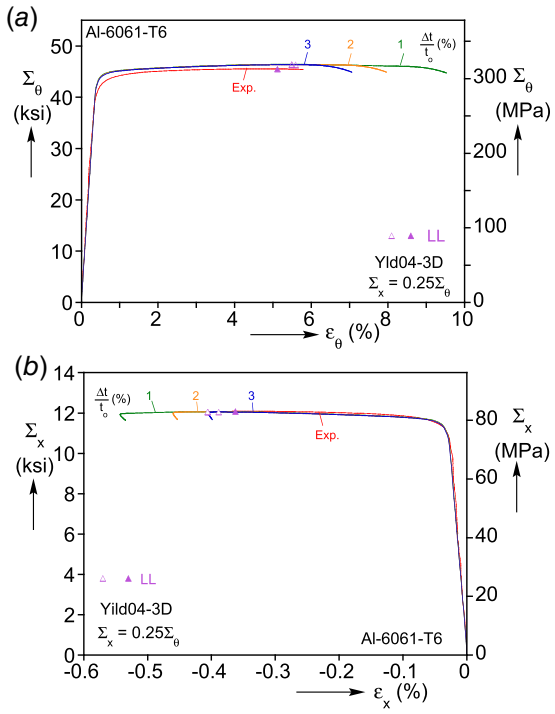

Fig. 11 Effect of imperfection amplitude on the stress-average strain responses for the $\eta = 0.25$ experiment using the Yld04-3D analysis: (*a*) hoop and (*b*) axial direction results

(F3D3 and F3D4). The symmetry planes at $x = 0$ and at $\theta = [0, \pi]$, and the tube inner surface define the cavity, which was closed with SFM3M3 surface elements at the thicker end. A volume increase is prescribed, and the corresponding pressure is used as a sensor. A user-amplitude routine (UAMP) takes the pressure and applies an appropriately scaled axial force to achieve the same radial path loading that was prescribed in the experiments, in accordance with Eqs. (1) and (2).

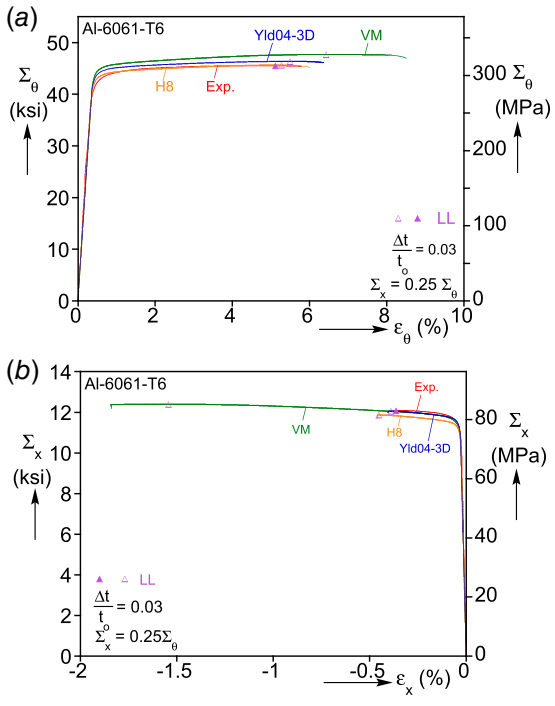

Fig. 12 Comparison of measured stress-average strain responses for $\eta = 0.25$ and predicted using the VM, H8, and Yld04-3D constitutive models: (*a*) hoop and (*b*) axial direction results

3.1 Simulation of $\Sigma_x = 0.25\Sigma_\theta$ Experiment. The experiment with stress ratio $\eta = 0.25$ is simulated numerically and the results are used to evaluate the performance of the model and provide additional insight into the localization of deformation that leads to burst. Figure 8(*a*) plots the calculated nominal hoop stress-average strain response using the Yld04-3D model and Fig. 8(*b*) the corresponding nominal axial response. For consistency with the experiments, the presented strains are computed from the average strain of all surface elements located in the same region over which strains were averaged in the experiment. An imperfection amplitude of $\Delta t = 0.03t_o$ is adopted. Included in the two figures are the responses recorded in the experiment. The agreement between the measured and calculated responses up to the limit loads is excellent in both figures. The calibrated constitutive model and the appropriate extraction of the material hardening play a pivotal role for this performance. The strains at the limit loads differ by a small amount but, while the descending part of the experimental hoop response reached an average strain of about 6% prior to burst, the analysis is taken further with the nominal stresses decreasing.

Figure 9(*a*) plots the equivalent strain in the neighborhood of the imperfection at $x = 0$ corresponding to the nine stations marked on the responses in Fig. 8 (the results are reflected about the plane of symmetry for better visualization). In profile 1 at $\varepsilon_\theta \approx 0.025$, the tube is deforming essentially uniformly so the increase in the strain in the center is directly related to the lower thickness of the imperfection. As the limit load is approached, deformation in the neighborhood of the imperfection accelerates (profile 2) and, by station 3 at the limit load, the strain has localized in the span of the imperfection ($2t_o$). At subsequent stations, the local strain grows reaching a maximum value of about 0.47 at station 9 when the calculation was terminated. Figure 9(*b*) shows a deformed image of the localizing part of the specimens corresponding to station 9. Superimposed color contours represent the strain level. The whole length of the imperfection zone sees higher strain but the more severe localization affects a length of about $0.5R$. The maximum strain occurs at $x = 0$ and decreases both in width and intensity away from this point, features that broadly agree with the localization image recorded by DIC in Fig. 6(*a*). The very rapid growth of the strain beyond the limit load is also illustrated

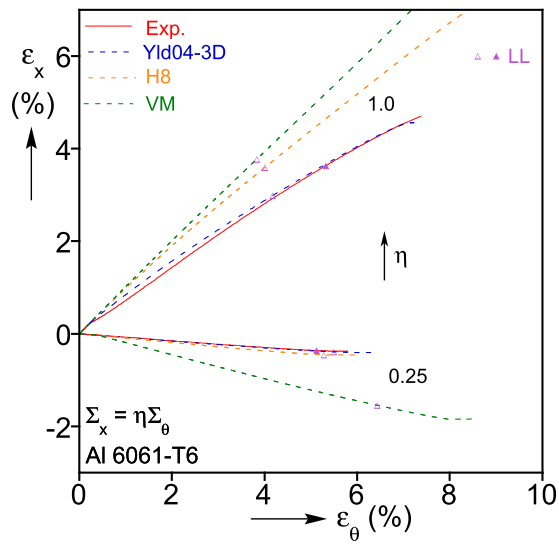

Fig. 13 Average strain paths traced experimentally for stress ratios of 0.25 and 1.0, and predictions using the VM, H8, and Yld04-3D constitutive models

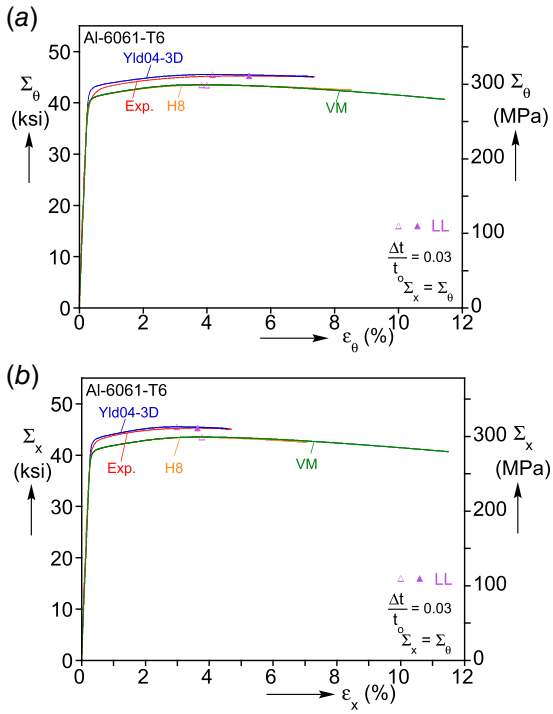

Fig. 14 Comparison of measured stress-average strain responses for $\eta = 1.0$ and predicted using the VM, H8, and Yld04-3D constitutive models: (*a*) hoop and (*b*) axial direction results

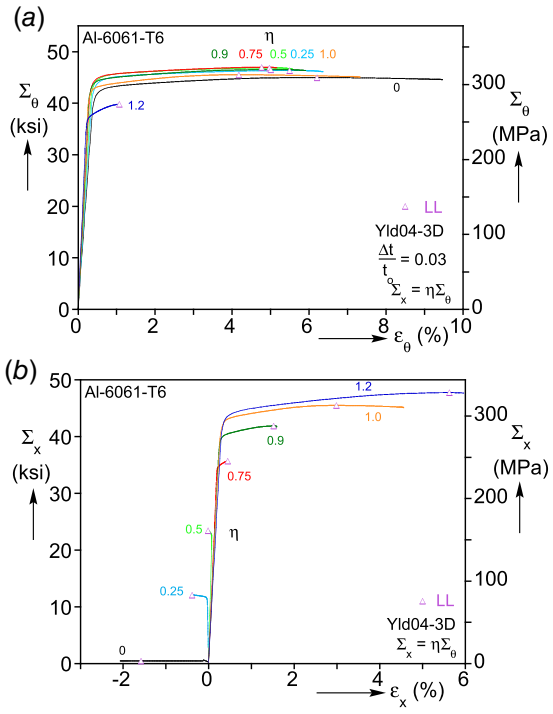

Fig. 16 Nominal stress-average strain responses for the seven P-T paths calculated using the Yld04-3D contitutive model: (*a*) hoop and (*b*) axial results

in Fig. 10, which plots the equivalent strain at the deepest point of the imperfection (0,0) versus the average hoop strain. Included here is the corresponding plot from the experiment, which follows a very similar trajectory, but terminates earlier due to failure by burst.

It is important to point out that experiments like the present ones tend to deviate somewhat from the ideal geometry and loading conditions in ways that include: specimen wall thickness eccentricity (Ξ_o in Table 1), surface roughness from manufacturing and machining, small internal defects, axial load eccentricity, etc. In analysis, the collective effect of these is typically represented by one geometric imperfection such as the wall thinning one used in the present study. In the way of assessing the effect of the geometry of the imperfection on the response, the amplitude of the imperfection $\Delta t/t_o$ was assigned values of {0.01, 0.02, 0.03}. The calculated nominal hoop and axial stress-average strain responses are plotted in Fig. 11 together with the experimental ones. Interestingly, the three pairs of responses are nearly identical up to their respective limit loads, which are also very close to each other. The main effect of the imperfection amplitude is on the post-limit load part of the response. Deceasing Δt results in slower growth of the strain in the localizing zone and stretches the response to higher average strains. The three responses in Fig. 11 were terminated when the maximum strain reached the level of configuration 9 in Fig. 9.

Figure 12 includes the nominal hoop and axial stress-average strain responses calculated using the VM and Hosford (H8) constitutive models, together with the stress–strain response extracted for each yield function from the uniaxial tension test as outlined in Appendix B (see Fig. 20(*b*)). The three simulations were terminated when the maximum strain in the necked region matched the last value recorded in the experiment just before burst (Fig. 4(*b*)). The H8 hoop response nearly matches the experiment whereas the

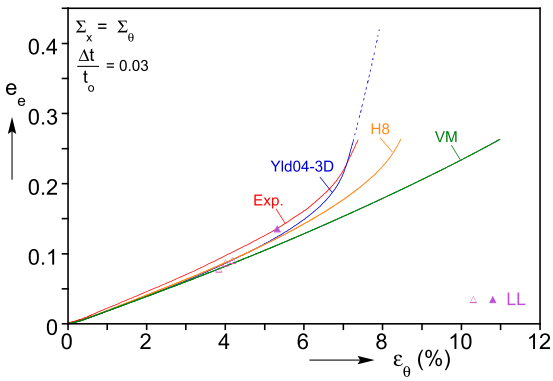

Fig. 15 Measured equivalent strain in the localizing zone versus the average hoop strain for $\eta = 1.0$ and corresponding predictions using the VM, H8, and Yld04-3D constitutive models

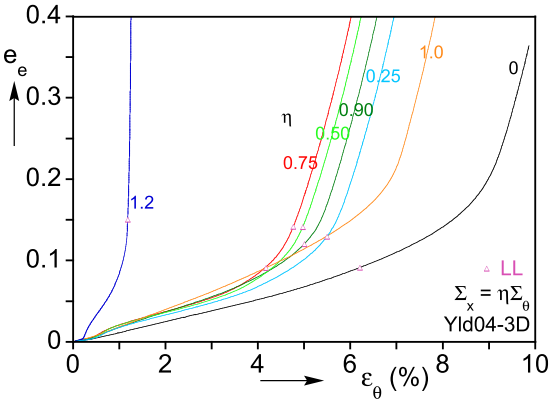

Fig. 17 Equivalent strain in the localizing zone versus the average hoop strain calculated using the Yld04-3D constitutive model for set of P-T radial paths—correspond to experimental results in Fig. 5

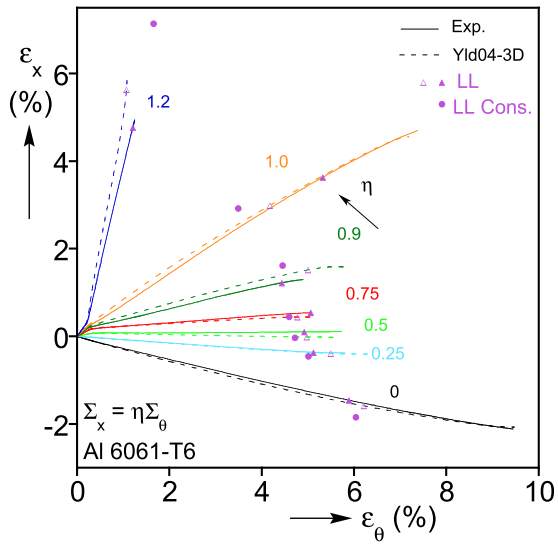

Fig. 18 Average strain histories for the set of P-T experiments and simulations using the Yld04-3D constitutive model. The bullets "•" represent the limit values predicted analytically in Appendix C.

axial response is slightly lower. The limit load is close to the experimental value and to the one of the Yld04-3D response, and so is the extent of the post-limit load response. The VM hoop response is higher than the experiment by about 2 ksi (14 MPa) but matches the axial response at least initially. The limit load occurs at larger ε_θ and the overall response extends to larger average strain. The axial response stretches to a strain that is nearly four times higher than the value of the experiment and those of the other two responses. As is apparent in Fig. 10, the growth of localization for VM is much slower than in the experiment and for the other two models. The cause of this discrepancy can at least be partly traced to the shape of the yield surface where it is intersected by the stress path $\Sigma_x = 0.25\Sigma_\theta$ in Fig. 19. The local normal is quite different from that of the H8 and Yld04-3D yield surfaces. This is also supported by the calculated strain paths in Fig. 13 where the path predicted by VM differs significantly from that of the experiment—see similar trend in the calculations of Ref. [4] who used shell elements to model their tubes.

3.2 Simulation of $\Sigma_x = \Sigma_\theta$ Experiment. For a broader presentation of the numerical effort, simulations results from the equibiaxial stress path $\Sigma_x = \Sigma_\theta$ are presented in Figs. 14 and 15. Figures 14(*a*) and 14(*b*) plot the nominal hoop and axial stress-average strain responses calculated using the three constitutive models for $\Delta t/t_o = 0.03$ together with the measured ones. In this case also, the Yld04-3D hoop and axial responses match the experimental ones very closely. By contrast, both sets of H8 and VM responses are somewhat lower. The limit loads of the three responses agree while the experimental limit load occurs at somewhat higher strain levels. Figure 15 plots the calculated equivalent strain at the deepest point of the imperfection (0,0) versus the average hoop strain—solid lines terminated at the maximum strain recorded in the experiment. Included is also the corresponding experimental trajectory. The Yld04-3D prediction matches well the measured trajectory but the localization is followed to much higher strain levels—partially drawn with dashed line. The H8 trajectory follows that of Yld04-3D up to the limit load, but the upswing in e_e occurs at higher average hoop strain. The VM solution has a hard time localizing even at very high values of ε_θ. The strain path predicted by this model included in Fig. 13 is also seen to deviate significantly from the measure one. Overall, the results confirm the inappropriateness of this constitutive model for response and failure calculations for Al-alloys (see similar conclusions in Giagmouris et al. [12] and Chen et al. [3]).

3.3 Summary of Numerical Simulations Results. All seven radial path experiments were simulated numerically and the nominal hoop and axial stress-average strain responses calculated using Yld04-3D are plotted in Figs. 16(*a*) and 16(*b*). An imperfection amplitude of $\Delta t/t_o = 0.03$ was adopted for the whole set. The responses follow the experimental ones in Fig. 3 to the same degree of agreement as for the two cases discussed in more detail in Figs. 8 and 14. The limit loads occur at strain levels comparable to those of the experiments. Figure 17 plots the equivalent strain at the deepest point of the imperfection (0,0) versus the average hoop strain for the seven simulations. The strain at the limit load is identified with the symbol r. All cases localize close to the onset of the limit load beyond which the local strain grows in a nearly exponential manner. The calculations were terminated when the local strain reached a value of 0.4. Although the figure does not facilitate one-to-one comparison with the experiments, the trend of the trajectories is similar to that of the corresponding measured results in Fig. 5 up to the points they were recorded. Such numerical results are essential for establishing the onset of failure using a suitably calibrated failure criterion such the triaxiality based Johnson and Cook [13], or more recent approaches that include the effect of shear (Lode angle) such as Mohr and Marcadet [14]. However, the localizing zone mesh may require further refinement when such calculations go deeper into the localization zone than in the present experiments and simulations.

Figure 18 compares the measured and calculated average strain paths using the Yld04-3D constitutive model for the whole set of experiments performed. The analysis reproduces the strain paths very well for all cases. By contrast, the VM model predictions were uniformly poor. The predictions for H8 showed improvement supporting the need for a nonquadratic yield function for plasticity of Al-alloys. Nevertheless, in concert with previous publications on the subject, for best performance the material anisotropy must be included in the constitutive model (e.g., Refs. [3–6,12]). It is worth mentioning that unlike other stress states considered in our broader study of ductile failure, here the Yld04-3D constitutive model was calibrated using only the pressure-tension experiments. The very good overall performance of predictions using this constitutive model attests also to the adequacy of the calibration performed for the present problem.

3.4 Analytic Prediction of Limit Load. The onset of localization denoted by a limit load instability is important for generating forming limits in manufacturing. The classical Considère condition for the limit load of thin-walled structures under uniform stress states can provide an analytical alternative to numerical treatment for establishing such critical states. Appendix C outlines the Considère condition for the present pressure-tension tube problem. The condition is formulated in terms of a general yield function, and is subsequently specialized to the three yield functions used in this study. The strains at the limit loads predicted using Yld04-3D for each of the seven radial loading paths are marked in Fig. 18 with symbol "•". For $0 \le \eta \le 0.9$, the predictions are close to both the experimental and the numerical values. Generally, they are slightly lower primarily because of the finite length of the test specimens. For $\eta = 1.2$, the prediction is rather higher. This is partly caused by the relatively poor match between the calibrated Yld04-3D surface in the neighborhood of this data point seen in Fig. 19. Better fitting of this part of the yield surface is expected to improve the limit strain prediction for $\eta = 1.0$ also. The limit strains predicted for the VM and H8 constitutive models are close to the numerically generated ones and consequently differ from the experimental values to the same degree. Interestingly, the predictions using $\sigma_x = \eta\sigma_\theta$ are close to the ones presented primarily because the strains at the limit load are relatively small.

4 Summary and Conclusions

The paper studies the response and failure of aluminum alloy tubes under combined tension and internal pressure with the aim of adding more clarity on the localization mechanism that leads to failure. Tubular specimens with $R/t \approx 16.7$ and $L/R = 4.77$ were loaded to failure in a custom setup under seven radial paths with $\Sigma_x/\Sigma_\theta = \eta = \{0.\ 0.25,\ 0.5,\ 0.75,\ 0{,}9,\ 1.0,\ 1.2\}$. All responses achieved load maxima beyond which deformation localized in an axial band with width of order of the wall thickness for six of the paths, and a circumferential band for $\eta = 1.2$. The deformation in the test section was monitored with high-resolution 3D DIC, both during the uniform and localized phases. Strains within the band grew rapidly and developed high gradients, reaching values nearly an order of magnitude larger than those outside the band. Failure occurred within the band suddenly for all specimens. The high resolution imaging enabled capture of the very rapid growth of deformation within the bands that preceded failure. However, because of the abruptness of localization, the actual strain at failure is much larger than the maximum strain recorded.

The experiments were simulated using a custom finite element analysis. Unlike our previous efforts on the subject, the tubes were discretized with solid elements. This enabled tracking the deformation in the localizing bands through the wall thickness to the high levels of strain required for the application of failure criteria. The analysis uses the von Mises and nonquadratic Hosford (H8) yield functions as well as the anisotropic yield function Yld04-3D calibrated for the stress state of the problem using the experimental responses. An important component of the analysis is the use of hardening responses extracted for each constitutive model from the necked zone of a tensile test using an inverse method.

The following conclusions are drawn from the study:

The analysis based on the calibrated Yld04-3D constitutive model is capable of accurately reproducing all aspects of the experimental behavior. This includes the initial uniform strain regime, the strains at the limit load instability, and the nearly exponential growth of strain in the subsequent localization in narrow bands. By contrast, the performance of the VM constitutive model was broadly poor. It failed to reproduce any of the initial strain paths, the predicted limit load strains are significantly off, and so is the evolution of localized deformation that follows. In the case of $\eta = 1.0$, VM failed to localize entirely. Switching to a nonquadratic yield function with exponent of 8, improved the prediction of some strain paths, resulted in better limit load predictions, and localizing zone strain trajectories closer to the measured ones.

The results demonstrate the following:

(a) The adoption of a nonquadratic yield function for failure predictions of Al-alloys is essential. Including the anisotropy in such a constitutive model produces more optimal results.
(b) Tracking the strains inside the narrow and high gradient localization zones necessary for prediction of failure requires a fine mesh of solid elements.
(c) Successful modeling of localizations requires a material hardening response extrapolated, for example, from the necked zone of a uniaxial tension test using the constitutive model adopted in the structural analysis.
(d) For structures under uniform stress states like the present one, the onset of a load maximum that precedes failure important in design can be estimated accurately using Considère type analysis. As in numerical analysis, this must be based on an appropriate yield function and the corresponding hardening response.

Acknowledgment

The authors acknowledge with thanks financial support received for this work from the National Science Foundation through the GOALI grant CMMI-1663269.

Conflict of Interest

There are no conflicts of interest.

Data Availability Statement

The datasets generated and supporting the findings of this article are obtainable from the corresponding author upon reasonable request. The authors attest that all data for this study are included in the paper.

Appendix A: Calibration of Yld04-3D

The Yld04-3D anisotropic yield function is calibrated using stresses and strains from the seven biaxial $\Sigma_x - \Sigma_\theta$ experiments performed and the uniaxial tension test as follows. For each of the biaxial tests, let $(\varepsilon_x^w,\ \varepsilon_\theta^w)$ be the strains corresponding to plastic work

$$W^p = \int_0^{\varepsilon_x^w} \sigma_x d\varepsilon_x^p + \int_0^{\varepsilon_\theta^w} \sigma_\theta d\varepsilon_\theta^p = 1000\ \text{psi}\ (6.9\ \text{MPa}) \tag{A1}$$

and $(\sigma_x^w,\ \sigma_\theta^w)$ be the corresponding stresses. This state of stress is introduced into the current yield function $\sigma_e = \Phi(\sigma_x^w,\ \sigma_\theta^w)$ and the following error function is developed

$$\mathcal{E}_\sigma = \left(\frac{\sigma_e}{\sigma_{xu}^w} - 1\right)^2 \tag{A2}$$

where σ_{xu}^w is the stress corresponding to the same value of plastic work measured in the uniaxial tension test. The measured instantaneous strain ratio $d\varepsilon_x^p/d\varepsilon_\theta^p$ is used to generate the R-ratio

$$R_{\text{exp}} = \frac{d\varepsilon_\theta^p}{d\varepsilon_r^p} = -\frac{1}{(1 + d\varepsilon_x^p/d\varepsilon_\theta^p)} \tag{A3}$$

The flow rule is then used to evaluate the same strain ratio at the required stress state

$$\left.\frac{d\varepsilon_x^p}{d\varepsilon_\theta^p}\right|_\Phi = \left.\frac{\partial\Phi/\partial\sigma_x}{\partial\Phi/\partial\sigma_\theta}\right|_{\sigma_x^w,\sigma_\theta^w} \tag{A4}$$

R_Φ is then generated as in (A3) and the strain ratio error function is formed:

$$\mathcal{E}_R = \left(\frac{R_\Phi}{R_{\text{exp}}} - 1\right)^2 \tag{A5}$$

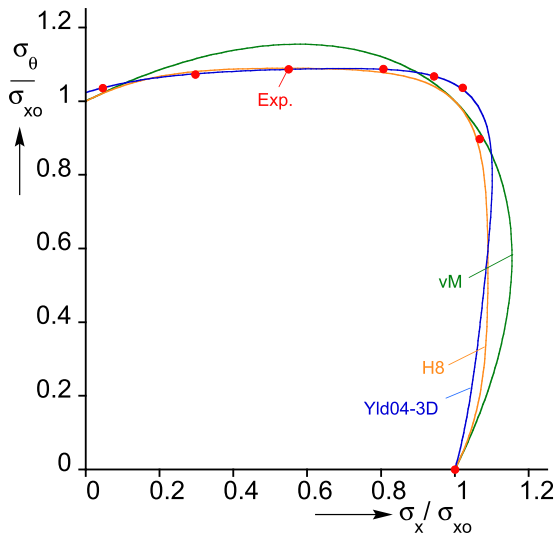

Fig. 19 Work contours of the VM, H8, and calibrated Yld04-3D constitutive models in the axial-hoop stress space together with experimental data points

The flow stress and R-value from uniaxial tension is incorporated in exactly the same manner. A global error function consisting of the weighted sum of the eight pairs of error functions is then generated

$$\mathcal{E}(c'_{ij}, c''_{ij}) = \sum_{i=1}^{8} \omega_{\sigma i}\left(\frac{R_\Phi}{R_{\exp}} - 1\right)^2 + \omega_{Ri}\left(\frac{\sigma_e}{\sigma^w_{xu}} - 1\right)^2 \tag{A6}$$

The basinhopping algorithm of the *Scipy* python package ([15]) was used to establish optimal values of the anisotropy coefficients (c'_{ij}, c''_{ij}) listed in Table 2. Because the stress states are limited to the (x, θ) space, six parameters could not be determined and are assigned values of 1.

A work contour of the calibrated constitutive model is shown in the axial-hoop stress space in Fig. 19 together with the experimental stresses (σ_{xo} is the uniaxial tension flow stress). Yld04-3D matches the experiments very well. Included are the corresponding work contours for the H8 and VM models. The quadratic yield function deviates from the data significantly. Hosford's yield function, H8, performs quite well but misses the data around the equibiaxial stress state.

Appendix B: Extraction of the Material Hardening at Large Strains

The material hardening response was extracted from a tensile test on a dog bone specimen extracted along the axis of the tube. The specimen necks at a strain of about 7% (see Fig. 20(*a*)). Thus, for higher strains the material hardening is extrapolated from the measured nominal stress–elongation response using the numerical simulation procedure of Tardif and Kyriakides [8] in conjunction with an appropriate constitutive model. Figure 20(*b*) shows the equivalent stress–strain responses extracted for the VM, H8, and Yld04-3D yield functions using this procedure. The three responses agree quite well up to a strain of about 10% but deviate for higher values with Yld04-3D exhibiting significantly more hardening, VM modest, and H8 somewhat more hardening. The dashed lines represent linear extrapolations using the tangent modulus at the end of the extraction process. Figure A2(*a*) shows that the experimental nominal stress–displacement response was matched by the numerical simulations for all three constitutive models. (More details about the specimen and model geometry and numerical procedure followed can be found in Scales [16]).

Appendix C: Analytical Estimates of the Limit Loads

Failure of a thin-walled tube loaded under combined internal pressure and axial load is preceded by a load maximum instability, which signifies the onset of localized deformation. Thus, the strains at the limit load represent a critical state, and analytical estimates provide useful alternatives to numerical treatment in manufacturing and other applications. Here, we develop the classical Considère condition for the onset of a load maximum in a thin-walled tube under combined internal pressure P and axial load F. Assume the tube to be finitely deformed to a radius r and wall thickness t, and that the elastic strains are negligibly small. The true stresses are given by

$$\sigma_\theta = \frac{Pr}{t} \quad \text{and} \quad \sigma_x = \frac{F}{2\pi rt} + \frac{Pr}{2t} \tag{C1}$$

In our experiments, the nominal stresses are

$$\Sigma_x = \eta \Sigma_\theta \tag{C2a}$$

Thus, at the load maximum

$$dP = 0 \quad \text{and} \quad dF = 0 \tag{C2b}$$

which, respectively, lead to

$$d\sigma_\theta = (2d\varepsilon_\theta + d\varepsilon_x)\sigma_\theta \quad \text{and} \quad d\sigma_x = (\sigma_\theta d\varepsilon_\theta + \sigma_x d\varepsilon_x) \tag{C3}$$

Let Φ be the yield function and σ_e the associated equivalent stress, then

$$d\sigma_e = \frac{\partial \Phi}{\partial \sigma_\theta} d\sigma_\theta + \frac{\partial \Phi}{\partial \sigma_x} d\sigma_x \tag{C4}$$

(C3) → (C4)

$$d\sigma_e = \left[\frac{\partial \Phi}{\partial \sigma_\theta}(2d\varepsilon_\theta + d\varepsilon_x) + \frac{\partial \Phi}{\partial \sigma_x}(\mathrm{d}\varepsilon_\theta + \frac{\sigma_x}{\sigma_\theta} d\varepsilon_x)\right]\sigma_\theta \tag{C5a}$$

Using the flow rule

$$d\sigma_e = \left[\frac{\partial \Phi}{\partial \sigma_\theta}\left(2\frac{\partial \Phi}{\partial \sigma_\theta} + \frac{\partial \Phi}{\partial \sigma_x}\right) + \frac{\partial \Phi}{\partial \sigma_x}\left(\frac{\partial \Phi}{\partial \sigma_\theta} + \frac{\sigma_x}{\sigma_\theta}\frac{\partial \Phi}{\partial \sigma_x}\right)\right]\Lambda\sigma_\theta \tag{C5b}$$

Plastic work compatibility requires that

$$d\varepsilon_e = \left(d\varepsilon_\theta + \frac{\sigma_x}{\sigma_\theta} d\varepsilon_x\right)\frac{\sigma_\theta}{\sigma_e} \tag{C6a}$$

and from the flow rule

$$d\varepsilon_e = \Lambda\left(\frac{\partial \Phi}{\partial \sigma_\theta} + \frac{\sigma_x}{\sigma_\theta}\frac{\partial \Phi}{\partial \sigma_x}\right)\frac{\sigma_\theta}{\sigma_e} \tag{C6b}$$

Combining (C5*b*) and (C6*b*) leads to the following Considère condition for the limit load

$$\left.\frac{d\sigma_e}{d\varepsilon_e}\right|_L = \sigma_{eL}\left[\frac{2\left(\frac{\partial \Phi}{\partial \sigma_\theta}\right)^2 + 2\frac{\partial \Phi}{\partial \sigma_\theta}\frac{\partial \Phi}{\partial \sigma_x} + \frac{\sigma_x}{\sigma_\theta}\left(\frac{\partial \Phi}{\partial \sigma_x}\right)^2}{\frac{\partial \Phi}{\partial \sigma_\theta} + \frac{\sigma_x}{\sigma_\theta}\frac{\partial \Phi}{\partial \sigma_x}}\right] \tag{C7}$$

where $\dfrac{\sigma_x}{\sigma_\theta} = \dfrac{1}{2} + \left(\eta - \dfrac{1}{2}\right)e^{-2\varepsilon_\theta}$.

For the material at hand $\varepsilon_{\theta L}$ is relatively small and thus $\sigma_x \approx \eta\sigma_\theta$.

Applying (C7) and this approximation to the von Mises yield function leads to

$$\left.\frac{d\sigma_e}{d\varepsilon_e}\right|_L = \sigma_{eL}\left[\frac{4\eta^3 - 6\eta^2 + 3\eta + 4}{4(\eta^2 - \eta + 1)^{3/2}}\right] \tag{C8}$$

Applied to the Hosford yield function with exponent 8 (C8) leads to

$$\left.\frac{d\sigma_e}{d\varepsilon_e}\right|_L = \sigma_{eL}\left[\frac{\eta[\eta^7 - (1-\eta)^7]^2 + 2[1+(1-\eta)^7](1+\eta^7)}{2^{1/8}\{\eta[\eta^7 - (1-\eta)^7] + [1+(1-\eta)^7]\}[\eta^8 + (1-\eta)^8 + 1]^{7/8}}\right] \tag{C9}$$

Application of (C8) to Yld04 requires numerical treatment.

It is worth pointing out that if in contrast to the nominal stresses being proportional (C2*a*), the true stresses are assumed to be proportional, $\sigma_x = \eta\sigma_\theta$, for pressure dominant loading paths the Considère condition becomes

$$\left.\frac{d\sigma_e}{d\varepsilon_e}\right|_L = \left(2\frac{\partial \Phi}{\partial \sigma_\theta} + \frac{\partial \Phi}{\partial \sigma_x}\right)\sigma_{eL} \tag{C10}$$

Appling the von Mises yield function to (C10) leads to

$$\left.\frac{d\sigma_e}{d\varepsilon_e}\right|_L = \frac{3\sigma_{eL}}{2(\eta^2 - \eta + 1)^{1/2}} \tag{C11}$$

(e.g., Mellor [17]).

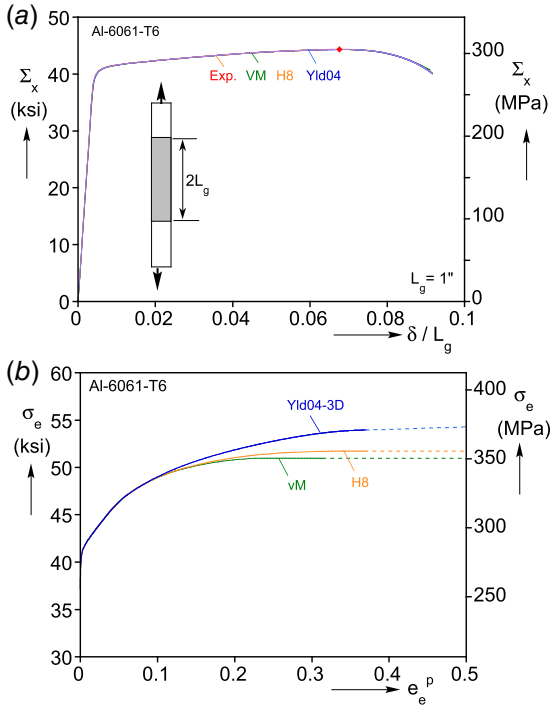

Fig. 20 (*a*) Comparison of nominal stress-elongation response measured in the experiment with ones reproduced numerically using the three constitutive models and (*b*) extracted true stress–plastic strain curves for the three constitutive models

Applied to the Hosford yield function with exponent 8 (C10) leads to

$$\left.\frac{d\sigma_e}{d\varepsilon_e}\right|_L = \frac{[\eta^7 + (1-\eta)^7 + 2]}{2^{1/8}[\eta^8 + (1-\eta)^8 + 1]^{7/8}}\sigma_{eL} \tag{C12}$$

Application of (C10) to Yld04 requires again numerical treatment.

The Considère expression (C7) was used to develop estimates of the limit loads for the seven stress path experiments reported using the VM, H8, and Yld04 yield functions. The equivalent stress and strain at the limit load can be evaluated using the material response extracted from the uniaxial test for each yield function using an inverse method that appears in Fig. 20(*b*). The stresses and plastic strains are then evaluated from the yield function and flow rule, respectively.

The total strains at the limit loads of the seven experiments for Yld04 are depicted with symbols "•" in Fig. 18—the elastic strain components were added for consistency with the experimental and numerical results.

References

[1] Scales, M., Tardif, N., and Kyriakides, S., 2016, "Ductile Failure of Aluminum Alloy Tubes Under Combined Torsion and Tension," Int. J. Solids Struct., **97–98**, pp. 116–128.

[2] Scales, M., Chen, K., and Kyriakides, S., 2019, "Material Response, Localization, and Failure of an Aluminum Alloy Under Combined Shear and Tension: Part I Experiments," Int. J. Plasticity, **120**, pp. 340–360.

[3] Chen, K., Scales, M., and Kyriakides, S., 2019, "Material Response, Localization, and Failure of an Aluminum Alloy Under Combined Shear and Tension: Part II Analysis," Int. J. Plasticity, **120**, pp. 361–379.

[4] Korkolis, Y. P., Kyriakides, S., Giagmouris, T., and Lee, L.-H., 2010, "Constitutive Modeling and Rupture Predictions of Al-6061-T6 Tubes Under Biaxial Loading Paths," ASME J. Appl. Mech., **77**(6), p. 064501.

[5] Kuwabara, T., Yoshida, K., Narihara, K., and Takahashi, S., 2005, "Anisotropic Plastic Deformation of Extruded Aluminum Alloy Tube Under Axial Forces and Internal Pressure," Int. J. Plasticity, **21**(1), pp. 101–117.

[6] Korkolis, Y. P., and Kyriakides, S., 2008, "Inflation and Burst of Aluminum Tubes Part II: An Advanced Yield Function Including Deformation-Induced Anisotropy," Int. J. Plasticity, **24**(9), pp. 1625–1637.

[7] Barlat, F., Aretz, H., Yoon, J. W., Karabin, M. E., Brem, J. C., and Dick, R. E., 2005, "Linear Transformation-Based Anisotropic Yield Functions," Int. J. Plasticity, **21**(5), pp. 1009–1039.

[8] Tardif, N., and Kyriakides, S., 2012, "Determination of Anisotropy and Material Hardening for Aluminum Sheet Metal," Int. J. Solids Struct., **49**(25), pp. 3496–3506.

[9] Korkolis, Y. P., and Kyriakides, S., 2008, "Inflation and Burst of Anisotropic Tubes for Hydroforming Applications," Int. J. Plasticity, **24**(3), pp. 509–543.

[10] Hosford, W. F., 1972, "A Generalized Isotropic Yield Criterion," ASME J. Appl. Mech., **39**(2), pp. 607–609.

[11] Dunand, M., Maertens, A. P., Luo, M., and Mohr, D., 2012, "Experiments and Modeling of Anisotropic Aluminum Extrusions Under Multi-Axial Loading–Part I: Plasticity," Int. J. Plast., **36**, pp. 34–49.

[12] Giagmouris, T., Kyriakides, S., Korkolis, Y. P., and Lee, L.-H., 2010, "On the Localization and Failure in Aluminum Shells Due to Crushing Induced Bending and Tension," Int. J. Solids Struct., **47**(20), pp. 2680–2692.

[13] Johnson, G. R., and Cook, W. H., 1985, "Fracture Characteristics of Three Metals Subjected to Various Strains, Strain Rates, Temperatures and Pressures," Eng. Fracture Mech., **21**(1), pp. 31–48.

[14] Mohr, D., and Marcadet, S. J., 2015, "Micromechanically-Motivated Phenomenological Hosford–Coulomb Model for Predicting Ductile Fracture Initiation at Low Stress Triaxialities," Int. J. Solids Struct., **67–68**(15), pp. 40–55.

[15] Pauli, V., and SciPy 1.0 Contributors, 2020, "SciPy 1.0: Fundamental Algorithms for Scientific Computing in Python," Nature Meth., **17**, pp. 262–272.

[16] Scales, M., 2019, "Localization and Failure of Aluminum 6061-T6 Under Biaxial Loading," Ph.D. dissertation, Engineering Mechanics, University of Texas at Austin, Austin, TX.

[17] Mellor, P. B., 1962, "Tensile Instability in Thin-Walled Tubes," J. Mech. Eng. Sci., **4**(3), pp. 251–256.